RSC Advances

PAPER

View Article Online
View Journal | View Issue

Cite this: *RSC Adv.*, 2025, **15**, 9576

Effect of Na^{2+} and Bi^{3+} substitution in lead-free BZT-Pr multifunctional ceramics for energy storage and thermal energy conversion

I. Zouari, *[ab] A. Dahri,[b] Z. Sassi,[c] L. Seveyrat,[c] N. Abdelmoula[b] and H. Khemakhem[b]

For this study, $Ba_{1-y-x}Pr_{2y/3}\square_{y/3}(Na_{0.5}Bi_{0.5})_xTi_{0.9}Zr_{0.1}O_3$ ($y = 0.5\%$; $x = 0.05$, 0.1 and 0.15) (abbreviated as BZT-Pr–*x*NBT) ceramics were prepared by a solid state reaction method. The samples were structurally characterized by X-ray diffraction (XRD) and the software Fullprof, which showed the atomic positions, bond distances, and bond angles of these materials in the tetragonal structure. The crystallite size, determined by both the Williamson–Hall and Debye–Scherrer methods, increases with increasing $Na_{0.5}Bi_{0.5}TiO_3$ (abbreviated as NBT) content in $Ba_{1-y}Pr_{2y/3}\square_{y/3}Ti_{0.9}Zr_{0.1}O_3$ ($y = 0.5\%$) (abbreviated as BZT-Pr) ceramic. The ultraviolet-visible (UV-Vis) diffuse reflectance spectrum indicated that the BZT-Pr–*x*NBT ceramics exhibited direct band gap values in the range of 2.90–2.78 eV. Moreover, this study investigates the ferroelectric, energy storage, and pyroelectric energy harvesting properties of BZT-Pr–*x*NBT ceramics with varying NBT contents ($x = 0.05$, 0.10 and 0.15). The results reveal that NBT substitution significantly influences the ferroelectric characteristics and enhances recoverable energy storage density (W_{rec}) and energy storage efficiency (η). Temperature-dependent scaling relations for the coercive field (E_C) and remnant polarization (P_r) were derived for all samples. For BZT-Pr–0.15NBT ceramic, the scaling relation for E_C and P_r ($E_C \propto T^{-0.089}$, $P_r \propto T^{-0.233}$) highlights improved thermal stability in this composition. Pyroelectric energy harvesting under the Olsen cycle identified BZT-Pr–0.05NBT as the most efficient composition. These findings emphasize the crucial impact of NBT substitution in optimizing the ferroelectric and pyroelectric properties of BZT-Pr–*x*NBT ceramics.

Received 10th January 2025
Accepted 23rd March 2025

DOI: 10.1039/d5ra00245a

rsc.li/rsc-advances

1. Introduction

Ferroelectric materials have gained significant technological and commercial importance over the past few decades, attracting growing interest due to their remarkable properties.[1–6] These include hysteresis, which enables their use in non-volatile memory;[7,8] high dielectric constants,[9,10] making them ideal for capacitors; and excellent high-temperature capacitance stability, crucial for automotive electronic systems such as multilayer ceramic capacitors.[11,12] Additionally, their narrow energy band gaps make them suitable for photocatalytic and optoelectronic applications,[13,14] while their high pyroelectric coefficients are valuable for infrared detection.[15,16] Furthermore, their exceptional energy conversion capabilities play a critical role in powering micro-electro-mechanical systems, demonstrating their versatility in a wide range of applications.[17–20] In all these fields and applications, lead-free materials have garnered increased attention in recent bibliographic studies due to significant environmental and health concerns.[21–25] Specifically, in the field of thermal energy conversion (pyroelectric energy harvesting) and energy storage, BCT–BZT ceramics,[26,27] Sr–BCTZ,[28–30] Sn–BSTZ ceramics,[31] and NBT–6BT–Sr compositions[32] are promising candidates.

In our previous works, we have already studied some physical properties of the $Ba_{1-y-x}Pr_{2y/3}\square_{y/3}(Na_{0.5}Bi_{0.5})_xTi_{0.9}Zr_{0.1}O_3$ ($y = 0.5\%$; $x = 0.05$, 0.1 and 0.15) (abbreviated as BZT-Pr–*x*NBT) system.[33] We have determined the lattice parameters of the compositions in their tetragonal structure, and we have observed an improved dielectric temperature stability with broadened curves due to a core–shell grain structure in these ceramics. Specifically, the dielectric study revealed that the BZT-Pr–0.15NBT composition meets the EIA X7R specification. In addition, a vibrational and photoluminescence study was conducted on these compositions. The analysis of hysteresis cycles, which demonstrate the ferroelectric properties of these materials, was limited to determining the remanent polarization and coercive field values for each composition.

In the present study, we will make a complementary study of the physical properties of this BZT-Pr–*x*NBT ($x = 0.05$, 0.1 and 0.15) system. Indeed, using X-ray diffraction (XRD) data, the

[a]*Laboratory of Nanomaterials and Systems for Renewable Energies (LaNSER) LR15CRTEn05, Research and Technology Center of Energy (CRTEn), Techno-Park Borj Cedria, Bp 95, Hammam-Lif, Tunis, 2050, Tunisia. E-mail: ilhem.zouari@crten.mesrs.tn*

[b]*Laboratory of Multifunctional Materials and Applications (LaMMA), LR16ES18, Faculty of Sciences of Sfax, University of Sfax, BP 1171, 3000 Sfax, Tunisia*

[c]*Univ Lyon, INSA-LYON, LGEF, EA682, Villeurbanne, F-69621, France*

atomic positions, bond distances, bond angles, and crystallite size have been determined. In addition, using UV-Vis analysis spectra, the optical band gaps have been calculated. Moreover, based on hysteresis loops data, the energy storage properties of these materials have been studied. Moreover, we analyze the temperature-dependent scaling relations for the coercive field (E_C) and remnant polarization (P_r) for all samples to study thermal stability. In addition, we undertake a more in-depth investigation of these cycles by examining the energy conversion process (pyroelectric harvesting energy) based on the Olsen cycle.

2. Experimental

Ceramics were prepared using the formula $Ba_{1-y-x}Pr_{2y/3}\square_{y/3}(Na_{0.5}Bi_{0.5})_xTi_{0.9}Zr_{0.1}O_3$ ($y = 0.5\%$; $x = 0.05$, 0.1 and 0.15) (abbreviated as BZT-Pr–xNBT) by the conventional solid-state reaction method. Stoichiometric amounts of $BaCO_3$, ZrO_2, TiO_2, Pr_6O_{11}, Bi_2O_3 and Na_2O_3 powders were weighed, mixed, calcined at 1150 °C for 12 h, and then pressed into discs which were sintered at 1300 °C for 4 h. X-ray diffraction (XRD) patterns were recorded at room temperature (RT) on an XPert Pro MPD diffractometer using CuKα_1 and CuKα_2 radiation (λ_1 = 1.540598 Å, λ_2 = 1.544426 Å). The results were processed by a Rietveld refinement using the software Fullprof in order to determinate the structure, cell parameters, atomic positions, bond angles and bond distances. The microstructure of the samples was examined using scanning electron microscopy (SEM) (Hitachi FlexSEM 1000) in secondary electrons (SE) mode at an accelerating voltage of 5 kV. UV-Vis diffuse reflectance spectra were obtained using a PerkinElmer Lambda 950 model. The optical band gaps of different compositions were estimated by extrapolation from Tauc plot of the Kubelka–Munk function.[34] Ferroelectric (P–E) loops were determined at different temperature (from 30 °C to 140 °C) by applying different electric field (1 kV mm^{-1}, 2 kV mm^{-1} and 3 kV mm^{-1}) at a frequency of 1 Hz. The current and electric field were measured during the application of cyclic electric fields, using a Keithley 428 current amplifier and a TREK Model 20/20C high-voltage amplifier.

3. Results and discussion

3.1 Structural and morphological properties

Using the software "Fullprof",[35] Rietveld refinements of the XRD patterns, at room temperature, were performed in the tetragonal structure ($P4mm$) for all compositions. The cell-parameters refinements, agreement factors, atomic positions, bond distances, and bond angles for the BZT-Pr–xNBT (x = 0.05, 0.1 and 0.15) ceramics are shown in Table 1. The refined XRD pattern of x = 0.1 composition, as an example, is shown in Fig. 1.

In addition, the crystallite size, determined by both the Williamson–Hall[36] and Debye–Scherrer[37] methods, are shown in Table 2. There is an increase of particle size, along with an increase of crystallinity observed by XRD, when the substitution of barium (Ba) by sodium (Na) and bismuth (Bi) increases from x = 0.05 to x = 0.15.

Table 1 Crystallographic data and agreement factors for BZT-Pr–xNBT compounds

	Compositions $Ba_{1-y}Pr_{2y/3}\square_{y/3}Ti_{0.9}Zr_{0.1}O_3$ (y = 0.5%)		
Cell parameters	x = 0.05	x = 0.1	x = 0.15
$a = b$ (Å)	4.021(0)	4.018(3)	4.017(1)
c (Å)	4.029(4)	4.024(1)	4.025(7)
V (Å^3)	65.147(8)	64.975(1)	64.96(1)
R_p	7.38	5.70	5.69
R_{wp}	9.80	7.52	7.36
R_{exp}	9.05	6.76	6.11
χ^2	1.17	1.24	1.45
Atomic positions (x; y; z)			
Ba/Na/Bi/Pr	0	0	0
	0	0	0
	−0.059(9)	0.001(5)	0.020(5)
Ti/Zr	0.5	0.5	0.5
	0.5	0.5	0.5
	0.4632(1)	0.526(8)	0.541(9)
O_1	0.5	0.5	0.5
	0	0	0
	0.4179(6)	0.473(3)	0.489(0)
O_2	0.5	0.5	0.5
	0.5	0.5	0.5
	−0.042(0)	0.003(5)	−0.003(7)
Bond angles (°)			
α [O_1–Ti–O_2]	84.818(3)	83.88(7)	83.953(4)
Bond distances (Å)			
O_1–Ti	2.0187(5)	2.020(6)	2.019(7)
Ti–O_2	2.0355(9)	2.105(6)	2.196(5)

As shown in Fig. 2a–c, the surface morphology of the compounds, examined using scanning electron microscopy (SEM) at a magnification of 2000×, reveals a relatively homogeneous microstructure with some porosity. There is a few small voids, suggesting the formation of highly densified

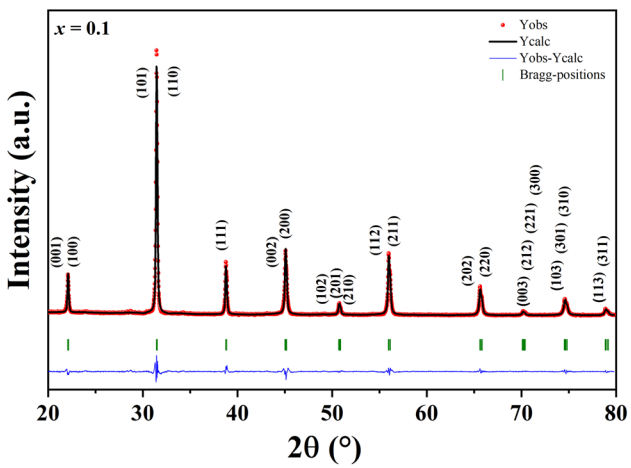

Fig. 1 Refined X-ray diffraction pattern of BZT-Pr–xNBT (x = 0.1) ceramic.

Table 2 Crystallite size determined by Debye–Scherrer formula (D_{SC}) and Williamson–Hall formula (D_{W-H}) for BZT-Pr–xNBT compounds

Compositions	D_{SC} (nm)	D_{W-H} (nm)
$x = 0.05$	26.52	48.29
$x = 0.1$	29.76	55.88
$x = 0.15$	35.27	63.57

homogeneous samples. Additionally, the analysis of grains on fractured fragments at a magnification of 4000×, as shown in Fig. 2d–f, indicates an average grain size between 0.5 μm and a few μm. We observe a slight increase in grain size with the NBT content, which is in good agreement with the increase in crystallite size as the NBT content increases.

3.2 Optical properties

For estimating the optical band gap from the ultraviolet-visible (UV-Vis) diffuse reflectance spectrum, the plot of $(F(R)h\nu)^2$ *vs.* $(h\nu)$ is shown in Fig. 3 for BZT-Pr–xNBT ($x = 0.05$) sample as an example. The values of the direct band gap obtained for the BZT-Pr–xNBT ($x = 0.05$, 0.1 and 0.15) ceramics are summarized in Table 3. These values are lower than those found in $BaTiO_3$ (BT) ceramics[38] and BZT ceramics.[39,40] In addition, with the increase of xNBT content, the value of the gap energy (E_g) decreased from 2.90 eV for $x = 0.05$ to 2.78 eV for $x = 0.15$. Indeed, the substitution of Ba^{2+} with Na^{2+} and Bi^{3+} can promote lower energy levels, allowing easier electronic transitions at lower energies.

3.3 Ferroelectric properties

Fig. 4a–c depict the *P–E* loops for BZT-Pr–xNBT ceramics with NBT contents of 5%, 10%, and 15%, respectively, measured under various electric fields at 30 °C and a frequency of 1 Hz. The results reveal that with increasing electric field, minor unsaturated *P–E* loops evolve into fully saturated loops. This transformation, which occurs above a certain threshold electric field, is a consistent phenomenon within finite frequency and temperature ranges.[41] The behavior is attributed to increases in the coercive field (E_C), maximum polarization (P_{max}), and remnant polarization (P_r), driven by domain growth and alignment under the applied electric field.

The data further indicate that increasing the NBT content results in a transition of the *P–E* loops from a wide profile, characterized by a high E_C at 5% NBT, to a slimmer profile. This suggests that NBT substitution is a viable strategy for optimizing materials for dielectric energy storage applications. The BZT-Pr–0.15NBT composition demonstrates a slim *P–E* loop with a nearly linear profile, indicative of high energy storage efficiency.[42] However, P_{max} decreases with increasing NBT content, a behavior attributed to the core–shell structure of the ceramics. The limited diffusivity of NBT into the BZT-Pr lattice, caused by chemical inhomogeneity, hinders the uniform alignment of domain walls and reduces the material's ferroelectric properties.[33,43] Previous studies have linked this reduction in ferroelectric properties to material losses resulting from local compositional fluctuations and random charge effects, which disrupt tetragonal symmetry and weaken ferroelectric order.[44]

Fig. 5a–c illustrate the temperature dependence of *P–E* hysteresis loops for BZT-Pr–xNBT ceramics ($x = 0.05$, 0.10, and 0.15), measured at 1 Hz under a constant electric field of 30 kV cm^{-1}. The hysteresis loops, recorded from room temperature to 140 °C, progressively become slimmer with rising temperature, tending toward a linear profile. This trend is confirmed by the ferroelectric parameters (P_{max}, P_r, ($\Delta P = P_{max} - P_r$), and E_C) extracted under the same conditions.

Fig. 6a–c show the thermal variation of P_{max}, P_r, and ΔP for $x = 0.05$, 0.10, and 0.15, respectively, while Fig. 6d compares E_C for all compositions. The results demonstrate a consistent

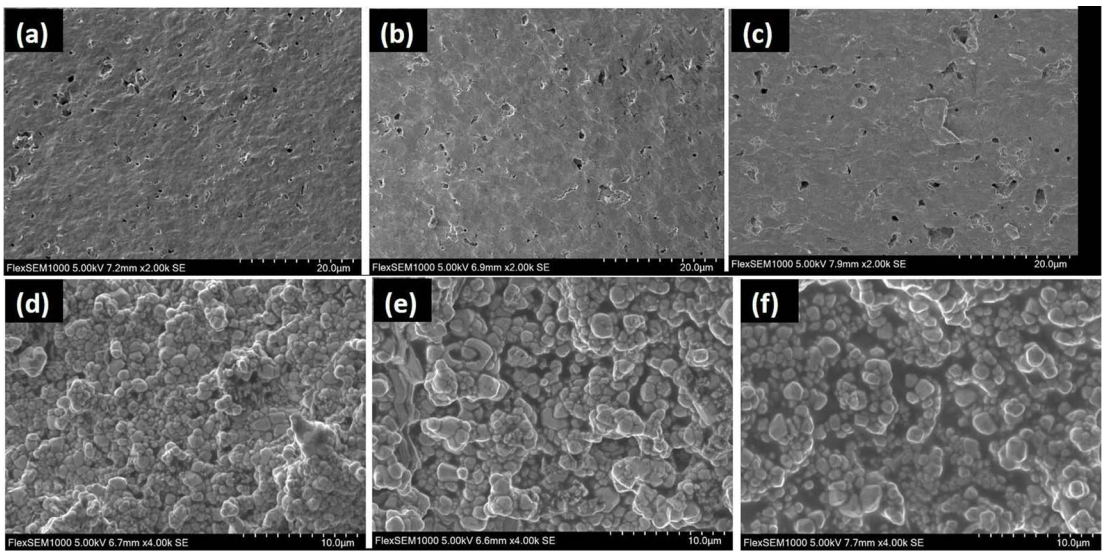

Fig. 2 Surface morphology and grain size analysis of BZT-Pr–xNBT samples: (a–c) surface morphology for $x = 0.05$, 0.10, and 0.15; (d–f) grain observation on fractured samples for $x = 0.05$, 0.10, and 0.15.

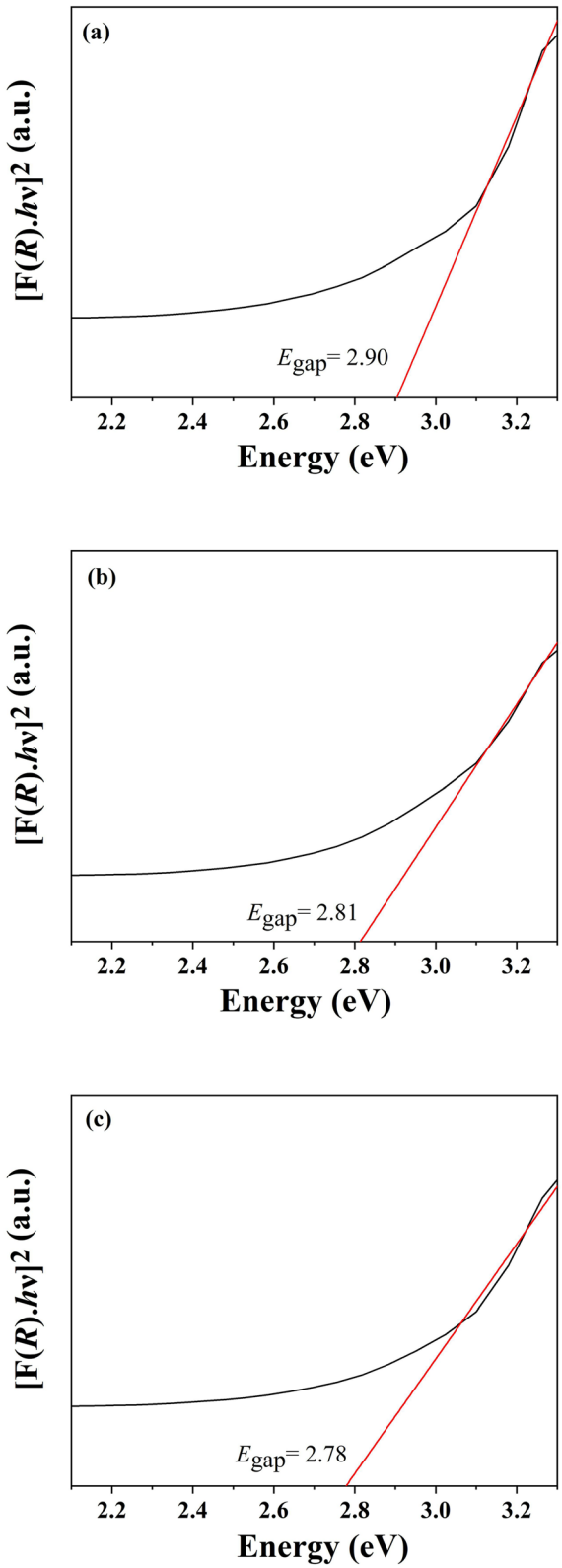

Fig. 3 UV-Vis spectrum for BZT-Pr–*x*NBT ceramics: (a) $x = 0.05$, (b) $x = 0.10$, and (c) $x = 0.15$.

decrease in P_{max}, P_r, and E_C with increasing temperature which is attributed to the degradation of ferroelectric performance above the Curie temperature (T_C) during the ferroelectric-to-

Table 3 Gap energies (E_g) of BZT-Pr–*x*NBT samples

Compositions	E_g (eV)
$x = 0.05$	2.90
$x = 0.1$	2.81
$x = 0.15$	2.78

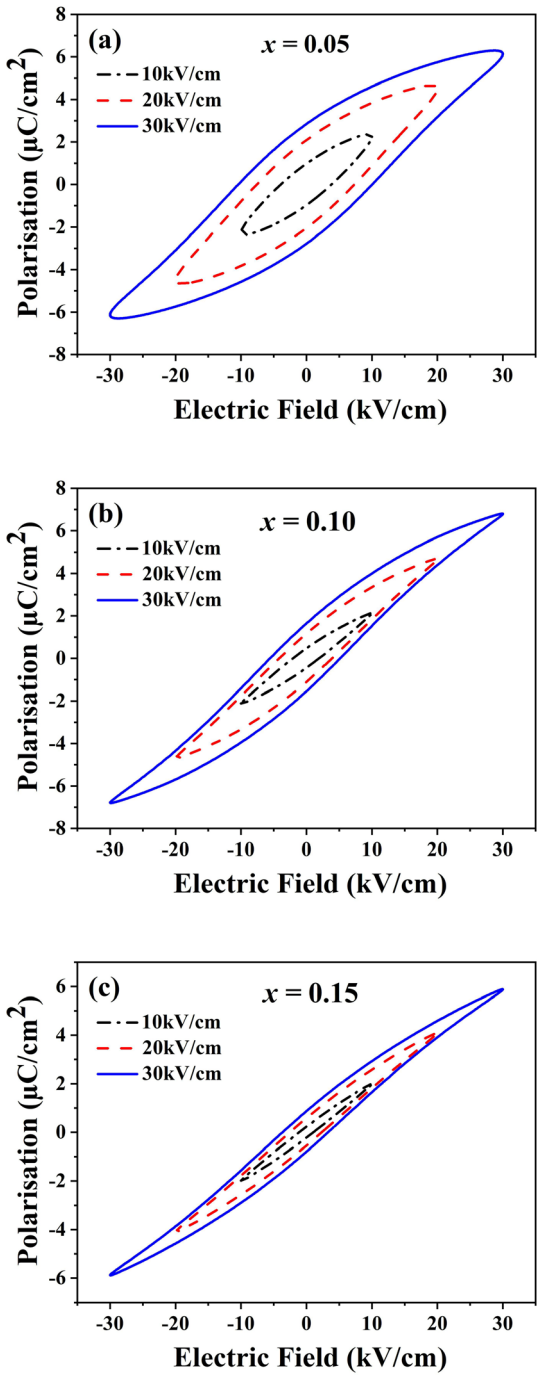

Fig. 4 Polarization *versus* electric field (*P*–*E*) hysteresis loops for BZT-Pr–*x*NBT samples at constant temperature (30 °C) for (a) $x = 0.05$, (b) $x = 0.10$, and (c) $x = 0.15$, measured under varying electric field magnitudes.

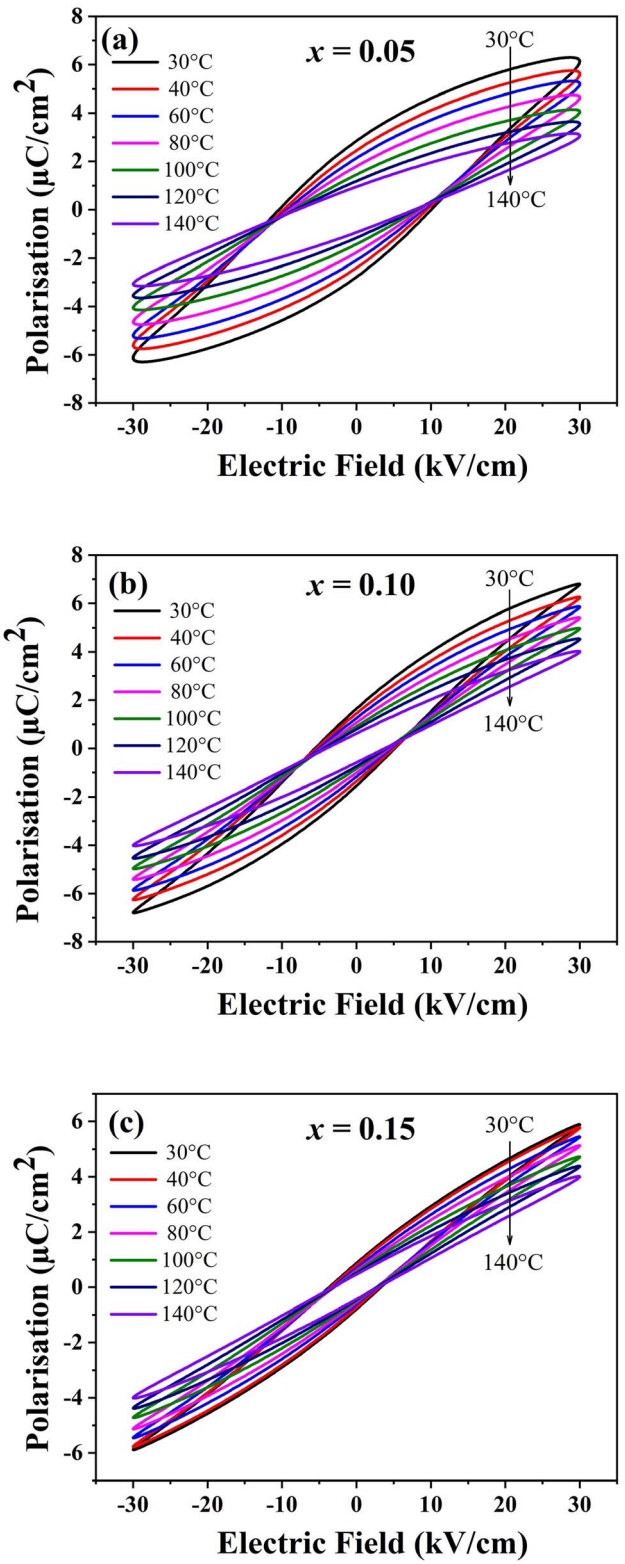

Fig. 5 Polarization *versus* electric field (*P*–*E*) hysteresis loops for BZT-Pr–*x*NBT samples as a function of temperature under a constant electric field of 30 kV cm^{-1} for (a) $x = 0.05$, (b) $x = 0.10$ and (c) $x = 0.15$.

paraelectric phase transition. This decline is linked to the breakdown of long-range domain order due to enhanced thermal fluctuations at elevated temperatures.[45]

Moreover, the comparison of E_C values highlights the impact of NBT substitution on ferroelectric properties. The composition with the lowest NBT content ($x = 0.05$) exhibits the highest E_C, reflecting a robust ferroelectric nature. Conversely, the composition with the highest NBT content ($x = 0.15$) shows the lowest E_C, indicative of a soft ferroelectric behavior which requires minimal electric field for domain switching.

3.4 Energy storage properties

Ferroelectric materials, renowned for their reversible spontaneous polarization, are highly efficient in energy storage and release, rendering them ideal candidates for energy storage applications.[46] Among these, relaxor ferroelectrics exhibit particularly high energy densities, making them increasingly prominent in advanced capacitors designed for high energy requirements and rapid charge–discharge cycles.[47] Building on this context, and considering the enhanced ferroelectric properties observed with NBT substitution, the subsequent section focuses on assessing the energy storage capabilities of BZT-Pr–*x*NBT ceramics with varying NBT content. This evaluation includes key parameters such as recoverable energy storage density (W_{rec}), total energy storage density (W_{tot}), and energy storage efficiency (η), derived from the analysis of their ferroelectric hysteresis loops.

The recoverable energy density, representing the energy released during the discharge process, can be evaluated from *P*–*E* hysteresis loop. This is determined by integrating the area between the discharge curve (the upper branch of the *P*–*E* loop) and the polarization axis, highlighted in green in Fig. 7a. Similarly, the total energy density, representing the energy stored during the charging process, corresponds to the area between the charge curve (the lower branch of the *P*–*E* loop) and the polarization axis. The relationship between these quantities is that W_{tot} is the sum of W_{rec} and the energy loss density (W_{loss}), with W_{loss} being the energy dissipated during the charging and discharging process. W_{loss} is calculated by integrating the area enclosed by the hysteresis loop, marked in orange in Fig. 7a.

These parameters are quantified using the following equations derived from the *P*–*E* loops, where *P* represents polarization, P_{max} is the maximum polarization, P_r is the remnant polarization, and *E* is the applied electric field:[48]

$$W_{rec} = \int_{P_r}^{P_{max}} E\mathrm{d}P \quad (1)$$

$$W_{Tot} = \int_{0}^{P_{max}} E\mathrm{d}P \quad (2)$$

For practical energy storage applications, energy storage efficiency (η) is a critical metric, defined as the ratio of W_{rec} to W_{tot}. This relationship is expressed as:

$$\eta = \frac{W_{rec}}{W_{Tot}} \times 100 = \frac{W_{rec}}{W_{rec} + W_{loss}} \times 100 \quad (3)$$

Higher efficiency (η) indicates minimal energy loss during charge and discharge cycles, which is crucial for reducing heat

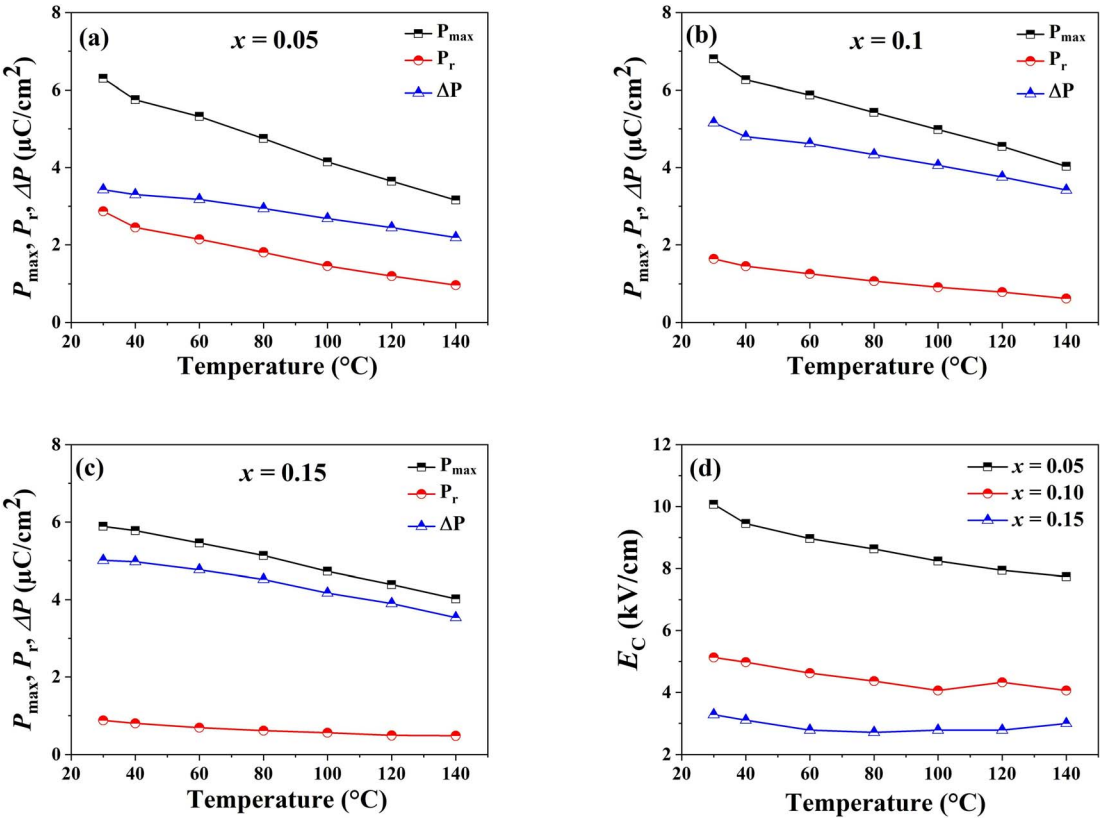

Fig. 6 Thermal variation of P_{max}, P_r and $\Delta P = (P_{max} - P_r)$, measured under an electric field of 30 kV cm^{-1} for (BZT-Pr–xNBT) samples with (a) $x = 0.05$, (b) $x = 0.10$ and (c) $x = 0.15$. In addition, panel (d) presents a comparison of the coercive field (E_C).

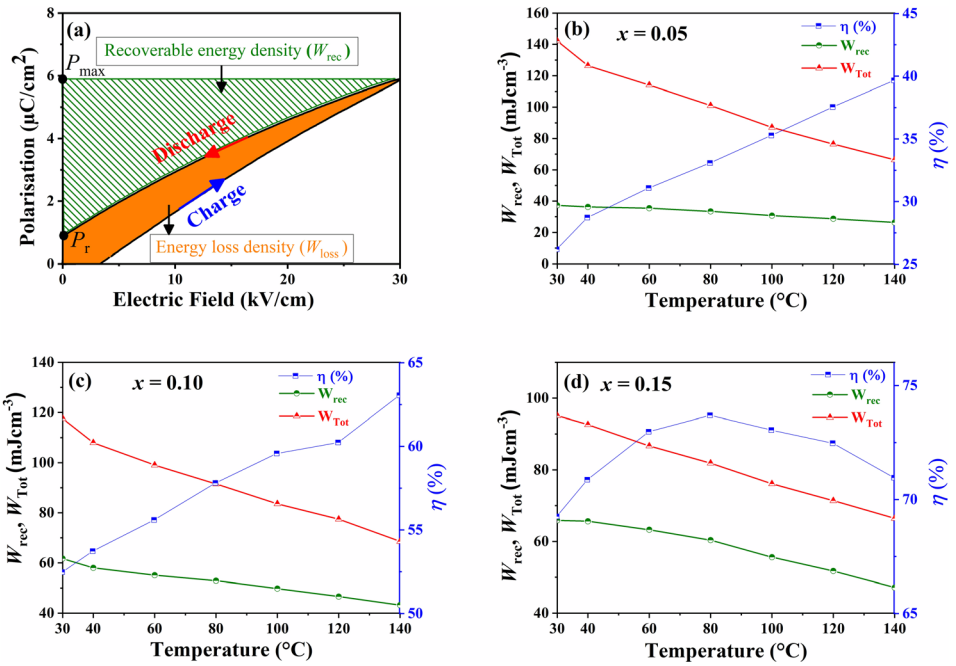

Fig. 7 (a) Schematic diagram illustrating the energy density of the BZT-Pr–0.15NBT sample during charging and discharging. Thermal variation of energy storage parameters measured under an electric field of 30 kV cm^{-1} for (BZT-Pr–xNBT) samples with (b) $x = 0.05$, (c) $x = 0.10$ and (d) $x = 0.15$.

generation and temperature rise within dielectric materials, thereby preserving the reliability and lifespan of capacitors.[49] Optimizing W_{rec} and η requires a larger ΔP and high dielectric breakdown strength, as these factors enhance energy recoverability and efficiency.[50]

The temperature-dependent energy storage parameters (W_{rec}, W_{loss}, and η) for BZT-Pr–xNBT ceramics with NBT contents of 0.05, 0.10, and 0.15, measured under a constant electric field of 30 kV cm^{-1} over a temperature range of 30 °C to 140 °C, are presented in Fig. 7b–d. At room temperature (30 °C), the BZT-Pr–5% NBT sample exhibits a coercive field (E_C) of 10.068 kV cm^{-1}, a recoverable energy density (W_{rec}) of 37.23 mJ cm^{-3}, and an energy storage efficiency (η) of 26.18%. Increasing the NBT content to 15% significantly reduces the coercive field to 3.28 kV cm^{-1}, while improving the ΔP value, resulting in a recoverable energy density of 65.86 mJ cm^{-3} and an efficiency of 69.25%. This enhancement in energy storage properties is attributed to the effects of NBT substitution, which modifies the ferroelectric characteristics of the material. This can be explained by the increase in grain size with increasing NBT content, as previously observed in the SEM analysis. In fact, a larger grain size can enhance energy storage properties by reducing the number of grain boundaries, which can trap charges.

As the temperature increases, the P–E loops become slimmer, reducing energy loss during charge–discharge cycles and yielding higher efficiency values. The maximum energy storage efficiency (η) at 140 °C is observed to be 39.66%, 63.05%, and 70.95% for NBT contents of 0.05, 0.10, and 0.15, respectively. These results clearly demonstrate that incorporating NBT significantly enhances the energy storage performance of BZT-Pr–xNBT ceramics, particularly at higher substitution levels. The slim-loop behavior of the BZT-Pr–15% NBT sample contributes to its relatively improved energy storage properties, most notably its thermal stability. This composition maintains an efficiency of approximately 70% over a wide temperature range, highlighting its potential for practical applications requiring consistent performance across wide temperature span.

3.5 The scaling behavior of hysteresis parameters

A comprehensive analysis of the scaling behavior of hysteresis parameters is crucial for understanding the interplay between temperature, electric field, and ferroelectric switching dynamics in BZT-Pr–xNBT. The coercive field and remnant polarization were evaluated as functions of temperature. Logarithmic plots of E_C *versus* ln(T) at various electric fields, shown in Fig. 8a–c, and logarithmic plots of P_r *versus* ln(T), presented in Fig. 9a–c, revealed a distinct dependence on the NBT content. Using the least squares linear fitting method, the relationship between E_C and T can be expressed as follows:[28,31]

$$\ln E_C = \alpha \ln T + Y_{EC} \quad (4)$$

Here, Y_{EC} represents the y-intercept, and α is the slope, both dimensionless constants. The intercept Y_{EC} becomes significant as T approaches absolute zero ($T = 0$). At $T = 0$, ferroelectric domains freeze, leading to behaviors distinct from those at elevated temperatures. While the impact of E_C at $T = 0$ is often

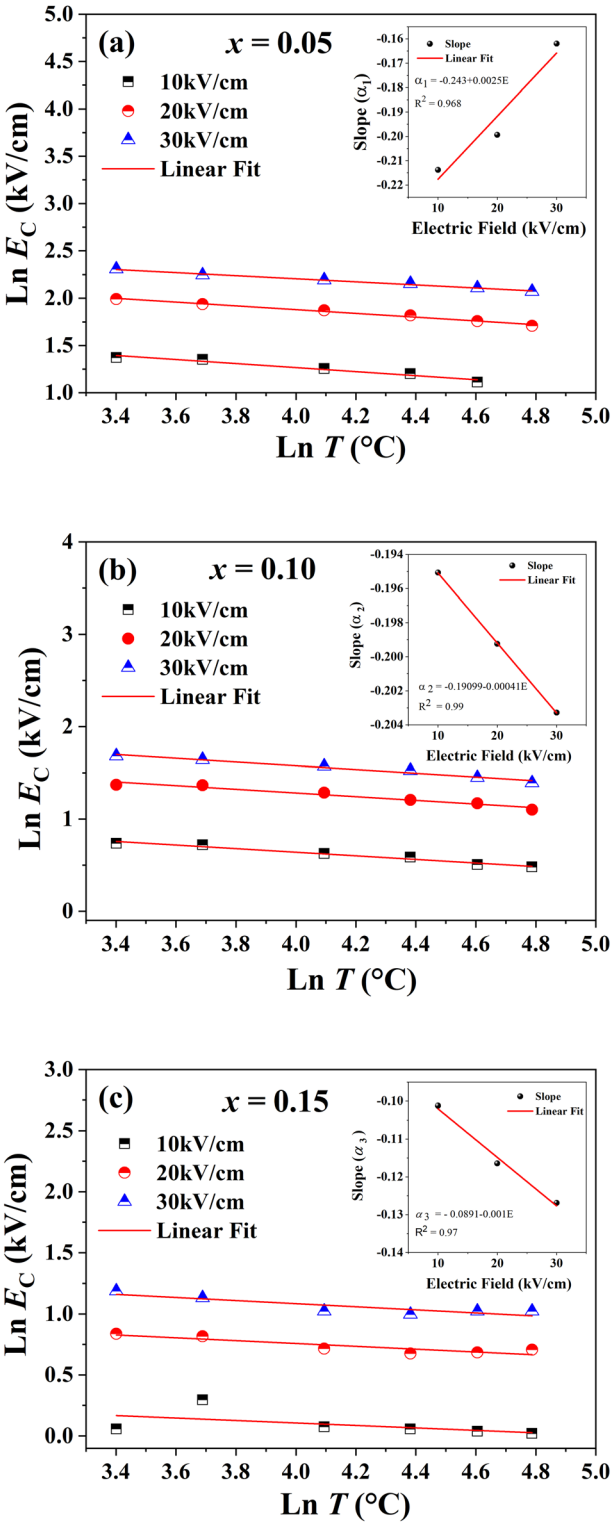

Fig. 8 Logarithmic plots of coercive field (E_C) *versus* temperature (T) under varying electric fields for BZT-Pr–xNBT ceramics with (a) x = 0.05, (b) x = 0.10 and (c) x = 0.15 and the insets show the slope variations with electric field.

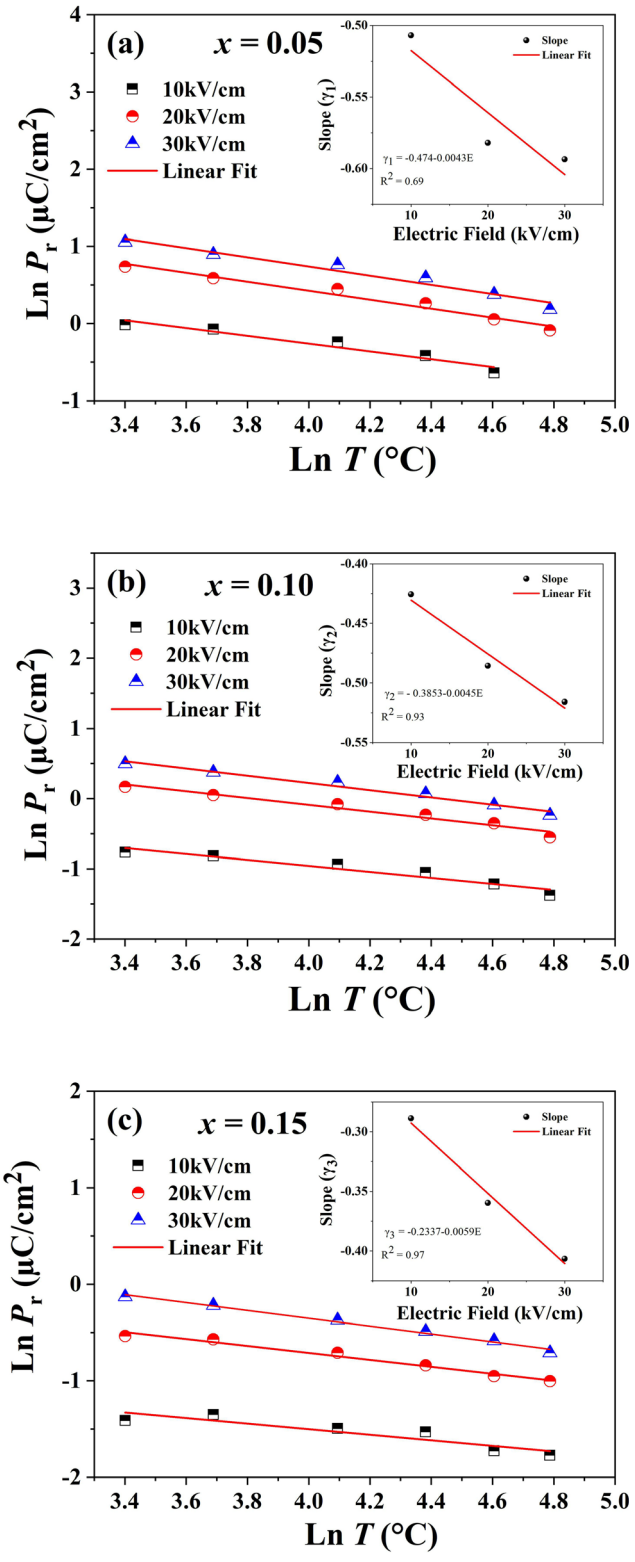

Fig. 9 Logarithmic plots of remnant polarization (P_r) *versus* temperature (T) under varying electric fields for BZT-Pr–xNBT ceramics with (a) $x = 0.05$, (b) $x = 0.10$ and (c) $x = 0.15$ and the insets show the slope variations with electric field.

disregarded in practical studies, Y_{EC} is retained for maintaining a linear fit. By rewriting eqn (4) in exponential form, the scaling relation can be expressed as:

$$E_C \propto T^{\alpha} \quad (5)$$

Similarly, the temperature dependence of the remnant polarization P_r can be described as:

$$\ln P_r = \gamma \ln T + Y_{Pr} \quad (6)$$

where γ represents the slope and Y_{Pr} denotes the y-intercept. This equation can also be transformed into its exponential form:

$$P_r \propto T^{\gamma} \quad (7)$$

For $x = 0.05$, the scaling relations were determined to be $E_C \propto T^{-0.243}$ and $P_r \propto T^{-0.474}$, indicating a relatively high temperature sensitivity for both parameters. As the NBT content increased to $x = 0.1$, the exponents reduced to $E_C \propto T^{-0.190}$ and $P_r \propto T^{-0.385}$, reflecting a moderate decrease in temperature dependence. At $x = 0.15$, the exponents further decreased to $E_C \propto T^{-0.089}$ and $P_r \propto T^{-0.233}$, indicating improved stability of both the coercive field and remnant polarization with temperature.

The evolution of the magnitudes of α and γ with increasing NBT content reflects the variation in domain dynamics with NBT substitution. At low NBT content ($x = 0.05$), the higher temperature sensitivity, as indicated by larger absolute values of α and γ, suggests a system where domain wall motion is more strongly influenced by thermal fluctuations, leading to increased mobility and switching activity. Conversely, at higher NBT content ($x = 0.15$), the reduced sensitivity implies a more stabilized domain structure, likely due to stronger domain wall pinning or reduced dipole rotation caused by NBT substitution.[28,31,51]

The results imply that BZT-Pr–xNBT with higher NBT composition ($x = 0.15$) is particularly suitable for environments requiring thermal stability. Furthermore, these findings align with energy storage investigations, underscoring the material's potential in practical applications where temperature resilience is critical.

3.6 Pyroelectric energy harvesting properties

Ferroelectric materials exhibit a characteristic hysteresis in their polarization–electric field behavior, which represents the energy required to polarize and depolarize the material. Typically, we observe this hysteresis in a counterclockwise loop, which enables the conversion of electrical energy into heat. However, by switching the cycle's orientation to a clockwise direction, this technique may be used for thermal energy harvesting. The Olsen cycle is designed to convert thermal energy into electricity. This process involves two isothermal and two isoelectric field stages.[52,53]

The Olsen cycle consists of four key phases[31,32] as depicted in Fig. 10:

In this cycle, the process begins by charging the material at a constant lower temperature (T_L) as the electric field increases from E_L to E_H, which results in an increase in polarization (phase 1–2). In the second stage (phase 2–3), heat (Q_S) is

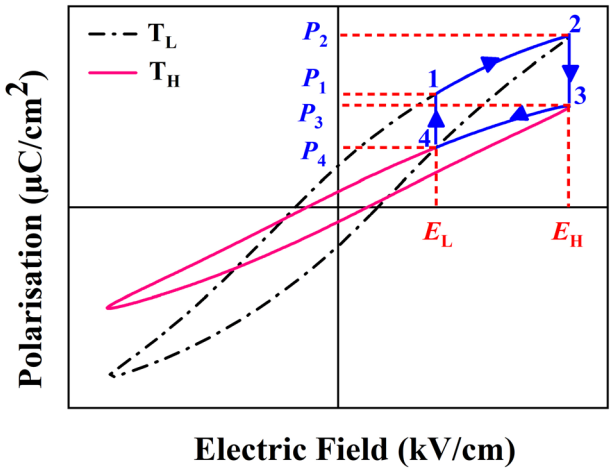

Fig. 10 Schematic representation of electrical energy conversion for BZT-Pr–0.10NBT sample as an example utilizing the Olsen cycle.

supplied to the material, raising its temperature from T_L to a higher value (T_H) while maintaining the electric field at E_H. As a result of this heat, the material depolarizes by producing a significant current that can be harvested. The third stage (phase 3–4) involves reducing the electric field from E_H to E_L while maintaining the material at T_H, which results in a weaker depolarization current. Finally, in the fourth stage (phase 4–1), heat is extracted at a constant electric field (E_L) which brings the material to its initial state at T_L and consequently completing the cycle.

The energy density produced in the cycle is determined by the area enclosed by the *P*–*E* loop, which can be quantified using the following equation:[28,31,32]

$$N_D = \oint E \mathrm{d}P \quad (8)$$

where E is the applied electric field, and dP is the change in polarization.

The thermal energy conversion potential of BZT-Pr–*x*NBT ceramics was investigated using the Olsen cycle under varying electric fields and temperature ranges. For compositions with NBT contents of 0.05, 0.10, and 0.15, the cycle was conducted with $E_L = 0$ kV cm^{-1} and $T_L = 30$ °C. As illustrated in Fig. 11a–d, energy density increases with greater electric field spans (E_H–E_L) and higher operating temperatures (T_H). The optimal composition, BZT-Pr–0.05NBT, achieved a maximum energy conversion of 80.77 kJ m^{-3} when operated between 30–140 °C and 0–30 kV cm^{-1}. In comparison, BZT-Pr–0.10NBT and BZT-Pr–0.15NBT exhibited lower energy densities of 64.42 kJ m^{-3} and 37.61 kJ m^{-3}, respectively. This reduction is attributed to the effects of NBT substitution, which altered the polarization response. Notably, a significant decrease in maximum polarization was observed for BZT-Pr–0.05NBT, explaining its superior energy conversion performance.[31] To highlight the performance of BZT-Pr–0.05NBT ceramics relative to other ferroelectrics reported in the literature, Table 4 provides

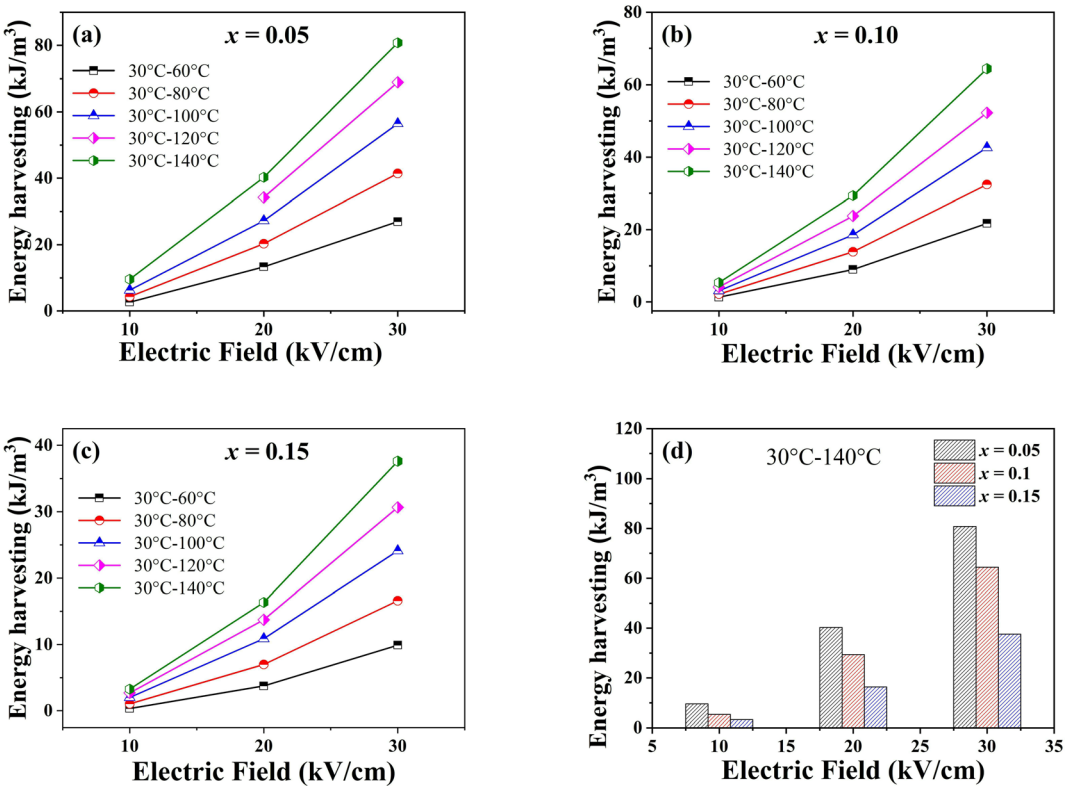

Fig. 11 Energy conversion *versus* electric field plots for (BZT-Pr–*x*NBT) samples with NBT content of (a) $x = 0.05$, (b) $x = 0.10$ and (c) $x = 0.15$ at $E_L = 0$ kV cm^{-1}. In addition, panel (d) compares the energy conversion capacity across the studied compositions.

Table 4 Energy density (N_D) of various ferroelectric materials

Materials	N_D (kJ m^{-3})	T_L–T_H (°C)	ΔT (°C)	E_L–E_H (kV cm^{-1})	ΔE (kV cm^{-1})	Ref.
BZT-Pr–0.05NBT	80.77	30–140	110	0–30	30	Current work
PZT	92	25–160	135	1–20	19	55
PZST	100	146–159	13	0–29	29	52
$Ba_{0.85}Ca_{0.15}Ti_{0.895}Fe_{0.005}Zr_{0.1}O_3$	101	30–110	80	0–10	10	54
$Ba_{0.85}Ca_{0.15}Ti_{0.895}Fe_{0.005}Zr_{0.1}O_3$	305	30–110	80	0–30	30	54
$Ba_{0.85}Ca_{0.15}Ti_{0.9}Zr_{0.1}O_3$	108	30–90	60	0–20	20	28
$Ba_{0.85}Sr_{0.15}Ti_{0.9}Zr_{0.1}O_3$	300	30–90	60	0–30	30	28
$(Ba_{0.95}Sr_{0.05})(Ti_{0.95}Zr_{0.05})O_3$	32	25–60	35	0–30	30	31
$(Ba_{0.95}Sr_{0.05})(Ti_{0.95}Zr_{0.05})_{0.975}Sn_{0.05}O_3$	175	25–110	85	0–30	30	31
$0.5Ba(Zr_{0.2}Ti_{0.8})O_3$–$0.5(Ba_{0.7}Ca_{0.3})TiO_3$	87	20–120	100	1–10	9	56

a comprehensive comparison of the energy harvesting capabilities of various ferroelectric materials using the Olsen cycle under different operating conditions. Table 4 shows that the response of BZT-Pr–0.05NBT ceramics is comparable to that of some materials. However, enhanced energy conversion capabilities have been observed in other modified ferroelectric compositions achieved through A-site or B-site substitution. For instance, adding 0.5% Fe to BCT–BZT–Fe ceramics improved the energy density and a maximum of 305 kJ m^{-3} was reached under conditions of 30–110 °C and 0–30 kV cm^{-1}.[54] Similarly, Sr substitution in BCT–BZT (BCT–BZT–Sr) resulted in a 200% increase in energy density, with 15% Sr yielding a maximum of 300 kJ m^{-3} over a 30–90 °C temperature range.[28] For BSTZS ceramics, substituting (Ti, Zr) with Sn significantly improved energy conversion, with a 5% Sn content achieving the highest energy density of 175 kJ m^{-3} under 25–110 °C and 0–30 kV cm^{-1}.[31] These findings highlight the critical role of composition tailoring in optimizing the thermal energy harvesting performance of ferroelectric materials.

4. Conclusion

To conclude, the structural, optical and ferroelectric properties of BZT-Pr–xNBT ($x = 0.05$, 0.10 and 0.15) ceramics, successfully prepared by a conventional solid-state reaction technique, were investigated. The atomic positions, bond distances, and bond angles of these compositions, which crystallized in the tetragonal structure, have been determined. Also, the crystallite size of each composition was calculated by two methods. Direct band gap values have been estimated using UV-Vis diffuse reflectance spectrum for these ceramics. Moreover, in this study, we systematically examined the ferroelectric and energy storage properties of BZT-Pr–xNBT ceramics with varying NBT contents ($x = 0.05$, 0.10 and 0.15) to evaluate their potential for energy storage and pyroelectric energy harvesting. Our findings reveal that increasing the NBT content significantly alters the ferroelectric characteristics of the material. Among the compositions, BZT-Pr–0.15NBT exhibited the highest energy storage properties at room temperature, with W_{rec} of 65.86 mJ cm^{-3} and η of 69.25%. This composition also demonstrated remarkable thermal stability across a wide temperature range (30–140 °C). Furthermore, the scaling relations for E_C and P_r as functions of temperature were derived. For E_C *versus* T, the scaling relations were determined as $E_C \propto T^{-0.243}$, $E_C \propto T^{-0.190}$ and $E_C \propto T^{-0.089}$ for samples with NBT contents of $x = 0.05$, $x = 0.10$ and $x = 0.15$ respectively. Similarly, the scaling relations for P_r *versus* T were $P_r \propto T^{-0.474}$, $P_r \propto T^{-0.385}$, and $P_r \propto T^{-0.233}$. These results indicate that BZT-Pr–0.15NBT exhibits improved thermal stability, with weaker temperature dependence of both E_C and P_r which justifies the high temperature stability of the sample. Additionally, the pyroelectric energy harvesting performance was assessed under the Olsen cycle. Among the compositions, BZT-Pr–0.05NBT demonstrated the highest energy conversion efficiency, making it a promising candidate for thermal energy harvesting applications. These results underscore the critical role of NBT substitution in tailoring the ferroelectric and pyroelectric properties of BZT-Pr–xNBT ceramics.

Data availability

The data that support the findings of this study are available from the corresponding author upon a reasonable request.

Conflicts of interest

There are no conflicts of interest to declare.

Acknowledgements

The authors acknowledge the support received from the Tunisian Ministry of Higher Education and Scientific Research.

References

1 T. Mikolajick, U. Schroeder and S. Slesazeck, *IEEE Trans. Electron Devices*, 2020, **67**, 1434–1443.
2 S. Gomasu, S. Saha, S. Ghosh, R. Bhowmik and D. Das, *ACS Appl. Mater. Interfaces*, 2024, **16**, 3654–3664.
3 P. K. Panda and B. Sahoo, *Ferroelectrics*, 2015, **474**, 128–143.
4 Y. Liu, Q. Li, L. Qiao, Z. Xu and F. Li, *Adv. Sci.*, 2022, **9**, 2204631.
5 S. Zhang, B. Malič, J. F. Li and J. Rödel, *J. Mater. Res.*, 2021, **36**, 985–995.

6 W. Ding, J. Lu, X. Tang, L. Kou and L. Liu, *ACS Omega*, 2023, **8**, 6164–6174.
7 J. Hoffman, X. Hong and C. H. Ahn, *Nanotechnology*, 2011, **22**, 254014.
8 Q. Yuan, F. Yao, Y. Wang, R. Ma and H. Wang, *J. Mater. Chem. C*, 2017, **5**, 9552–9558.
9 R. Ahmed, R. Si, S. ur Rehman, Y. Yu, Q. Li and C. Wang, *Results Phys.*, 2021, **20**, 103623.
10 H. Chen, C. Yang, C. Fu, J. Shi, J. Zhang and W. Leng, *J. Mater. Sci.: Mater. Electron.*, 2008, **19**, 379–382.
11 Y. Yuan, S. R. Zhang, X. H. Zhou, B. Tang and B. Li, *J. Electron. Mater.*, 2009, **38**, 706–710.
12 H. I. Hsiang, L. T. Mei and Y. J. Chun, *J. Am. Ceram. Soc.*, 2009, **92**, 2768–2771.
13 V. Batra, S. Kotru, M. Varagas and C. V. Ramana, *Opt. Mater.*, 2015, **49**, 123–128.
14 Y. Qi, L. Zhang, G. Jin, Y. Wan, Y. Tang, D. Xu and D. Sun, *Ferroelectrics*, 2014, **458**, 64–69.
15 Y. Bai, T. Siponkoski, J. Peräntie, H. Jantunen and J. Juuti, *Appl. Phys. Lett.*, 2017, **110**, 063903.
16 L. Tang, S. Han, Y. Ma, Y. Liu, L. Hua, H. Xu and J. Luo, *Chem. Mater.*, 2022, **34**, 8898–8904.
17 V. Segouin, M. Domenjoud, Y. Bernard and L. Daniel, *Acta Mater.*, 2021, **211**, 116870.
18 V. Athikesavan, S. Bhuvana and G. Thilakavathi, *Ferroelectr. Lett. Sect.*, 2022, **49**, 104–110.
19 D. Thuau, K. Kallitsis, F. D. D. Santos and G. Hadziioannou, *J. Mater. Chem. C*, 2017, **5**, 9963–9966.
20 M. Valant, *Prog. Mater. Sci.*, 2012, **57**, 980–1009.
21 L. F. Zhu, B. P. Zhang, L. Zhao and J. F. Li, *J. Mater. Chem. C*, 2014, **2**, 4764–4771.
22 S. Khardazi, H. Zaitouni, S. Belkhadir, D. Mezzane, M. Amjoud, Y. Gagou and S. Terenchuk, *J. Solid State Chem.*, 2022, **311**, 123112.
23 M. Maraj, W. Wei, B. Peng and W. Sun, *Materials*, 2019, **12**, 3641.
24 S. K. Upadhyay, V. R. Reddy, P. Bag, R. Rawat, S. M. Gupta and A. Gupta, *Appl. Phys. Lett.*, 2014, **105**, 112907.
25 G. Liu, W. Yu, Y. Wang, H. Feng, M. Hao, G. Wu and Y. Yan, *Ceram. Int.*, 2023, **49**, 34387–34396.
26 A. P. Sharma, D. K. Pradhan, S. K. Pradhan and M. Bahoura, *Sci. Rep.*, 2019, **9**, 16809.
27 A. Mandal, D. Yadav, S. K. Mittal, U. Jamwal, D. Kaneria, A. Khokhar and K. L. Yadav, *J. Alloys Compd.*, 2024, **995**, 174817.
28 S. Patel, D. Sharma, A. Singh and R. Vaish, *J. Materiomics*, 2016, **2**, 75–86.
29 C. Zhou, Q. Zhang, W. Cai, R. Yang, S. Chen, R. Gao and J. Sun, *Mater. Sci. Semicond. Process.*, 2022, **150**, 106950.
30 W. Cai, Q. Zhang, C. Zhou, R. Gao, S. Zhang, Z. Li and C. Fu, *J. Mater. Sci.: Mater. Electron.*, 2020, **31**, 9167–9175.
31 I. Djemel, M. H. Khedhri, I. Kriaa, Z. Sassi, L. Seveyrat, N. Abdelmoula and H. Khemakhem, *Appl. Phys. A*, 2023, **129**, 784.
32 I. Kriaa and A. Maalej, *J. Energy Storage*, 2024, **102**, 114044.
33 I. Zouari, Z. Sassi, L. Seveyrat, N. Abdelmoula, L. Lebrun and H. Khemakhem, *J. Alloys Compd.*, 2020, **825**, 153859.
34 J. Tauc, Optical properties and electronic structure of amorphous semiconductors, in *Optical Properties of Solids: Papers from the NATO Advanced Study Institute on Optical Properties of Solids Held*, Springer US, Boston, MA, at Freiburg Germany, 1966, pp. 123–136.
35 J. Rodriguez-Carvajal, A Rietveld and Pattern Matching Analysis Program (Version April 2008), Laboratoire Léon Brillouin (CEA-CNRS), France, 2008.
36 G. K. Williamson and W. H. Hall, *Acta Metall.*, 1953, **1**, 22–31.
37 J. Kanamori, *J. Appl. Phys*, 1960, **31**, S14–S23.
38 H. Bai and X. Liu, *Mater. Lett.*, 2013, **100**, 1–3.
39 T. Badapanda, S. Sarangi, B. Behera, P. K. Sahoo, S. Anwar, T. P. Sinha and L. S. Cavalcante, *Curr. Appl. Phys.*, 2014, **14**, 708–715.
40 C. C. Parhi, A. B. Thirumalasetty, A. R. James and M. Wuppulluri, *ACS Omega*, 2023, **8**, 37752–37768.
41 S. Patel, A. Chauhan and R. Vaish, *Int. J. Appl. Ceram. Technol.*, 2015, **12**, 899–907.
42 M. K. Bilal, J. Wang, R. Bashir, H. Liu, S. U. Asif, J. Xie and W. Hu, *J. Am. Ceram. Soc.*, 2021, **104**, 3982–3991.
43 Y. Sun, H. Liu, H. Hao, S. Zhang, L. Guo and Z. Yu, *Ceram. Int.*, 2012, **38**, S41–S44.
44 H. I. Humburg, M. Acosta, W. Jo, K. G. Webber and J. Rödel, *J. Eur. Ceram. Soc.*, 2015, **35**, 1209–1217.
45 K. Chen, J. Ma, J. Wu, X. Wang, F. Miao, Y. Huang, C. Shi, W. Wu and B. Wu, *J. Mater. Sci.: Mater. Electron.*, 2020, **31**, 12292–12300.
46 N. Li, K. Xie and H. Huang, *ACS Energy Lett.*, 2023, **8**, 4357–4370.
47 A. R. Jayakrishnan, J. P. B. Silva, K. Kamakshi, D. Dastan, V. Annapureddy, M. Pereira and K. C. Sekhar, *Prog. Mater. Sci.*, 2023, **132**, 101046.
48 Q. Li, W. Zhang, C. Wang, L. Ning, Y. Wen, B. Hu and H. Fan, *J. Alloys Compd.*, 2019, **775**, 116–123.
49 F. Z. Yao, Q. Yuan, Q. Wang and H. Wang, *Nanoscale*, 2020, **12**, 17165–17184.
50 M. Zhou, R. Liang, Z. Zhou, S. Yan and X. Dong, *ACS Sustain. Chem. Eng.*, 2018, **6**, 12755–12765.
51 S. Patel, A. Chauhan, A. Chauhan and R. Vaish, *Mater. Res. Express*, 2015, **2**, 035501.
52 R. B. Olsen, D. A. Bruno and J. M. Briscoe, *J. Appl. Phys.*, 1985, **58**, 4709–4716.
53 R. B. Olsen and D. A. Bruno, Pyroelectric conversion materials, in *IECEC 1986, Proceedings of the Twenty-First Intersociety Energy Conversion Engineering Conference*, 1986, vol. 1, pp. 89–93.
54 D. Sharma, S. Patel, A. Singh and R. Vaish, *J. Asian Ceram. Soc.*, 2016, **4**, 102–111.
55 S. Patel, A. Chauhan and R. Vaish, *Mater. Res. Express*, 2014, **1**, 025504.
56 G. Vats, A. Chauhan and R. Vaish, *Int. J. Appl. Ceram. Technol.*, 2015, **12**, E49–E54.